Characteristics of the Turkana Low-Level Jet Stream and the Associated Rainfall in Cmip6 Models

oscar lino (linowanjala@gmail.com)
University of Nairobi https://orcid.org/0000-0001-6690-8271

Mutemi J. Nzau
University of Nairobi

Dyer Ellen
University of Oxford Hooke Library: University of Oxford

Opijah Franklin
University of Nairobi

James Rachel
University of Bristol

Washington Richard
University of Oxford

Tom Webb
York University

Research Article

Keywords: urkana low-level Jet stream, ERA5, CMIP6, atmospheric models, East Africa rainfall

Posted Date: January 27th, 2022

DOI: https://doi.org/10.21203/rs.3.rs-1250203/v1

Abstract

The Turkana low-level jet stream (TJ) is important to climatic conditions over northern Kenya and East Africa. The representation of the TJ in climate models varies due to the TJ interaction with Turkana channel that is influenced by model resolution and influences the model representation of the regional climate. This study compares features of the TJ in CMIP6 AMIP model simulations with ERA5. Models reveal wind speeds that match those of the reanalysis from the ERA5 at the jet entrance (13 m/s) but lower magnitudes of wind speed and vertical shears compared to ERA5 within the Turkana channel. The models with slowest wind speeds, have a flattened Turkana channel and fail to exhibit the terrain constriction at 37°E which otherwise aids in accelerating winds to form a jet core. Furthermore, they fail to represent the narrowing of the channel as in ERA5, thereby forming blocking walls in the channel, forcing vertical ascent and mixing, and weakening shear. Stronger ascent is conducive for rainfall formation, enhancing wet anomalies by up to 8% above the observed climatology at the exit of the TJ when the jet stream is weaker. By applying a new narrowing index, we demonstrate the need to improve topography details in the CMIP6 models, particularly those with resolution coarser than 1.5°, in order to properly simulate the TJ and the observed rainfall over the northwestern areas of eastern Africa.

1 Introduction

Over northern Kenya, there exists a low-level jet stream which has great socio-economic potential for the region, as well as being an important mechanism for moisture transport from the western Indian Ocean to some interior parts of northwestern East Africa (Vizy and Cook, 2019; Nicholson, 2014). This fast-flowing current of air, which is now called the Turkana low-level Jet stream (TJ), gained recognition among aviators who frequently experienced turbulence when landing and taking off from the region (Indeje et al., 2001). The understanding of the TJ benefited from short field campaigns by Kinuthia and Asnani (1982) and Kinuthia (1992). The mean monthly wind speeds in range 10 to 13 m/s culminate at 850 mb (Nicholson, 2016) from January to December. Occasional ascents of pilot balloons during field campaigns in Kinuthia (1992) indicated the TJ is strongest during late night and early morning, with associated wind speeds in the range of 30 to 50 m/s. The TJ is fragmented into two branches in the channel which merge at the mid-portion of the channel to form a jet core (Kinuthia and Asnani, 1982; Indeje et al., 2001). Previous studies have related the TJ to the observed aridity over parts of Eastern Africa (Trewartha 1981; Flohn, 1964; Griffiths, 1972; Nicholson, 1996; Nicholson 2016). It is for this reason that the inclusion of the TJ in dynamical models is important to the representation of rainfall over the northern Kenya region (Sun et al., 1999; Indeje et al. 2001; King et al., 2021).

Eastern Africa (EA) is a generally dry region, found in an otherwise wet equatorial belt (Camberlin, 2018). The region is hyper-arid at the tip of the Horn and near the Egyptian border with annual rainfall below 150 mm (Njenga at al., 2014), an apparent extension of desert conditions from the bordering middle-East and Sahara respectively. An extensive area featuring less than 400 mm annual rainfall stretches from eastern Ethiopia through northwestern Kenya, to Lake Turkana (Nicholson, 2016; Camberlin, 2018). Extreme drought events have been common, exacerbated by modes of variability that perturb rainfall received,

whose manifestations have increased notably since 2005. Between 2015 and 2016, drought prevailed over most parts of Ethiopia related to El Nino conditions (Sjoukje et al 2015), while 2016 and 2017 exhibited drought over the Greater Horn related to La Nina (Uhe et al., 2015). Similarly, three drought events occurred in the seven years alone (2005/2006, 2008/2009, 2010/2011) compared with only seven events in 30 years (1975 to 2004). The increased manifestation of drought impacts has heightened interests in climate information from models to inform disaster risk management and increase people's adaptive capacity to climate extremes (Nicholson, 2014; Kilavi et al., 2018).

Analysis of observations, reanalysis, and climate models has led to understanding of the TJ and its influence on the climate in East Africa. Increased studies on the TJ using the current generation of climate models and improved datasets can lead to a more quantitative understanding of the TJ as well as its impacts. The aridity is linked to regional topography and wind flow. Due to the north-south orientation of the east African highlands, advection of moist air from Congo-basin into the arid area is blocked (Slingo et al., 2005). Lower-tropospheric (at 850 mb level) divergence matched by subsidence at mid troposphere characterizes the arid sub-regions (Yang et al., 2015). The large-scale divergence is linked with the TJ as fast-moving winds cause a drop in pressure due to Bernoulli effect (Indeje et al., 2001) and interact with terrain within the channel, inducing frictional divergence (Ba and Nicholson, 1998). The divergence in the lower atmosphere favors stable atmospheric conditions and a dry climate over the plain and low plateau over coastal Tanzania, Kenya and Somali border, to the Nile plains of Sudan and South Sudan (Nicholson, 2016). The TJ also transports large amounts of moisture that promote rainfall formation at the jet exit in western parts of South Sudan and Ethiopia during the northern summer (Vizy and Cook, 2019). The strength of the TJ covaries with the ENSO system that drives rainfall over East Africa during October to December (Sun et al., 1999; King et al., 2021).

Acosta and Huber (2017) examine the ability of the Community Atmosphere Model to correctly simulate low-level jets over the Indo-Gangetic Plain, and found the model had a good representation, which they attribute to proper representation of model physics schemes that explicitly resolve the Indo-Asian monsoon. Investigating the NCAR model at a grid resolution of 0.5°, Indeje et al., (2001) reported a fairly good representation of the features in the TJ compared with the observations in Kinuthia (1992). A comparison of how several climate models simulate the TJ has been made, indicating that the models follow similar seasonal pattern as the ERA5 and MERRA2 reanalysis with more comparable values from January to May than in the remaining months of the year in CMIP5 (King et al., 2021). While in the seasonal cycle the TJ is strong during the two major rainfall seasons in East Africa (March to May and October to December), its strong anomalies are accompanied by dry conditions in its area of influence. Munday et al. (2020) suggests that the CMIP5 models with horizontal resolution of more than 60 km do not replicate the associated dry anomalies as finer grid lengths are required to accurately simulate the TJ and its interaction with East African climate. However, reasons for why the models represent the TJ the way they do, including the influence of the TJ on the airflow over the region, and how this affects the weather over the region in models, is not well understood. Furthermore, there have been no previous studies of the simulation of the TJ in the newest generation of global models.

This work focuses on characteristics of the TJ in CMIP6 models. Specifically, it discusses model representation of the strength, structure and position of TJ along the Turkana channel which may affect the simulated rainfall. We recognize that model simulation of these features introduces a measure of uncertainty because of the lack of observational datasets. But since it is understood that some low-resolution models ignore low-level jet streams (Acosta and Huber, 2017), there is the opportunity to refine our understanding of the jet stream characteristics and influence on rainfall by using the recently available CMIP6 and ERA5 with high spatial resolution. The current work will investigate the following a) What are the climatic characteristics of the TJ in different climate models? b) How might resolution and the representation of topography in the models be related to these differences? c) Is the simulated rainfall related to these differences?

Atmospheric models and reanalysis datasets used, as well as methods for locating and quantifying key features of the jet stream are described in section 2. Results from analysis that characterize the TJ in CMIP6 models, associate the simulated TJ to topography and relate rainfall in CMIP6 to the TJ are shown in section 3. A summary is provided in section 4 and conclusions drawn in section 5.

2 Data And Methods

2.1 Datasets

This study makes use of the data from the sixth iteration of the Coupled Model Intercomparison Project (CMIP6: Eyring et al., 2016) under the World Climate Research Programme (Taylor et al. 2012). The historical Atmospheric Model Intercomparison Project (AMIP), which is one of the four baseline experiments from CMIP6, were considered for a period between 1981 to 2014. Twenty-six atmospheric models (Table 1) were analyzed, which were the models with all variables needed for this analysis. The historical AMIP runs were chosen for this analysis as they assume the historical sea surface temperature (SST) input into the experiments. Consequently, they may reduce uncertainties related with SST feedback (Eyring et al. 2016) and allow for oscillations in the output data to be matched with the atmospheric reanalysis datasets. The resolution of the models differs but the analysis was performed on the models' native grid to preserve the original information.

Table 1
Name and description of CMIP6 models used in this study. Marked 1 are models from the High-Resolution Model Intercomparison Project. Marked 2 are regular experiment models

MODELING CENTER	MODEL	Atmospheric horizontal resolution (lat x lon,°)
AS-RCEC	TaiESM1[2]	0.94×1.25
BCC	BCC-ESM1[2]	1×1.25
	BCC-CSM2-MR[2]	0.94×1.25
CAMS	CAMS-CSM1-0[2]	0.94×1.25
CAS	FGOALS-g3[2]	1.39×1.41
	FGOALS-f3-L[2]	1.39×1.41
CCCma	CanESM5[2]	1.39×1.41
CNRM-CERFACS	CNRM-CM6-1[1]	0.56×0.83
	CNRM-ESM2-1[2]	1.25×1.88
CSIRO	ACCESS-CM2[2]	1.25×1.88
	ACCESS-ESM1-5[2]	1.25×1.88
INM	INM-CM5-0[2]	5.18×2
	INM-CM4-8[2]	1.85×1.88
IPSL	IPSL-CM6A-LR[1]	1.11×1.13
MPI-M	MPI-ESM1-2-HR[1]	1.11×1.13
MIROC	MIROC6[2]	1.5×2
MOHC	HadGEM3-GC31-LL[2]	1×1.25
	HadGEM3-GC31-MM[1]	0.93×0.94
MRI	MRI-ESM2-0[2]	1.11×1.13
NCAR	CESM2[2]	1.89×2.5
NCC	NorESM2-LM[2]	1.27×2.5
	NorCPM1[2]	1.89×2.5
NOAA/GFDL	GFDL-CM4[2]	0.94×1.25

MODELING CENTER	MODEL	Atmospheric horizontal resolution (lat x lon,°)
NUIST	NESM3[2]	2.77×2.81
SNU	SAM0-UNICON[2]	2.77×2.81

To benchmark the findings by the models, this study takes advantage of the latest reanalysis dataset from the fifth version of European Centre for Medium-Range Weather Forecasts reanalysis - ERA5 (Hersbach et al., 2019). In ERA5, the 2000 to 2017 climatological wind speeds associated with the TJ matches well with structures found using NCEP CFSR reanalysis dataset (Hartman 2018), and MERRA2 dataset (Vizy and Cook 2019). However, the climatological wind speeds in the ERA5 are comparable, albeit slower than 31 m/s that was occasionally recorded in the July 1979 to June 1980 single year of field observations in Kinuthia (1992). This disparity is hypothesized to be as result of terrain features of smaller scale that are not resolved in the reanalysis at the horizontal resolution of 0.25°.

2.2 Methods

We discuss the methodology in terms of the seasonal cycle of the TJ, its spatial structure, the detection threshold of the TJ, the index for shape of the Turkana channel, and the precipitation index.

The seasonal shift in the direction of the TJ is determined by assessing the prevailing wind vectors over East Africa, which shift direction from southerly to northerly, following the apparent movement of the overhead sun in a year. The horizontal extent of the TJ was identified in both the reanalysis and models by masking the mean wind for speed of magnitudes less than 5 m/s. While the choice of the 5 m/s is arbitrary, the resultant wind vectors at the 850 mb level provided a key map showing the relatively high-speed winds with an axis confined within the Turkana channel in ERA5 and most of CMIP6 models. This matched the observational work of Kinuthia and Asnani (1992) who reported that the TJ culminates in the layers 925 and 700 mb with wind speeds of about 13 m/s within the Turkana channel.

The location and structure of the TJ is determined in vertical wind profiles for the cross section through the Turkana channel, which is at the point 2°S, 43°E to the point 8°N, 32°E. Those points were used by Nicholson (2016) to mark the cross-sections. In this work, the TJ exit coincided with a point beyond which the wind was slower than 5 m/s. The winds accelerate in the mid-portion of the Turkana channel particularly in October to May season depicting a jet core. Finally, the jet entrance marked the point of entry of winds into the Turkana channel.

The threshold of the occurrence of the TJ was identified when the structures of the cores of the TJ in the model matched those in the ERA5 datasets. A search criterion was applied to the wind speed at 37°E, 3°N for mean JJAS seasons over the period of 35 years to identify optimal thresholds for a strong and well-formed TJ. In the process, values in range between 6 m/s and 12 m/s were considered as maximum wind speeds at 850 mb level, matched by wind speeds above that maximum decreasing by values in range 2 m/s and 6 m/s by the point of minimum wind speeds is realized before reaching 500 mb level. The

Optimum threshold for the TJ during JJAS in the models is that which the majority of the models, especially those of higher resolution with a well-formed Turkana channel (described by index of narrowing) that maintains it. The thresholds applied in studying the TJ using ERA-Interim dataset of maximum wind speed 10 m/s, matched with decreasing wind speeds aloft in 2-4 m/s (Nicholson, 2016) and those postulated by Oliviera et al., (2018), were found too stringent to capture a TJ in the models.

The TJ is associated with topography through the shape of the Turkana channel. The shape is described using the narrowing index estimated as the mean change in the cross-sectional area of the channel. The cross-sectional area was obtained by estimating the area under a curve between constant 850 mb and the surface below the pressure level along a longitude. The cross-sectional area was calculated along each longitude for the longitudes 33°E (marking the exit of the jet stream) to 42°E (marking the entrance of the jet stream), and bounded by the latitudes 2°S and 9°N. The Turkana channel is the largest topographic feature below the 850 mb level, with floor at 700 m (Camberlin, 2018) within the domain bounded by those coordinates. The narrowing index summarizes the consistency in narrowing towards the constriction at the mid-portion of the Turkana channel, and indicates the relative ease of air mass to flow through the channel without being blocked and being accelerated to form an intense TJ core in accordance with Bernoulli's principle (Indeje et al., 2001).

A precipitation index is computed for climatological precipitation associated with the TJ in CMIP6 models. The index is obtained as composite means of TJ occurrences, and no-TJ occurrences for rainfall for each grid box. These TJ events were isolated from the 35 years of analysis by identifying when the core wind speeds in the TJ reached the detection threshold of the TJ which were achieved during JJAS season. This season matches when moisture is high at the TJ exit region as it is the main rainfall season over the north-western parts of East Africa (Camberlin 2018).

3 Results

3.1 Seasonal cycle of the TJ in CMIP6 model climatology

Presence of the TJ throughout the year is investigated by masking wind vectors for winds speeds below 5 m/s at 850 mb level. The pressure level is chosen since the wind here flows above the terrain and therefore, it is the lowest level of the TJ which is free from obstruction by the terrain barrier. Figure 1 (panels a to c) shows the mean wind vectors in ERA5 versus wind from 2 CMIP6 models chosen to illustrate two contrasting models. High wind speeds of at least 5 m/s in both ERA5 and the HadGEM-GC31-LL are constrained within the Turkana channel throughout the year. The BCC-ESM1 model has the winds spread out over Kenya.

Through the year, the prevailing wind direction shifts from southerly during May to September, to northerly during October to April. The southerly flow during May to September splits over northern Kenya, into two streams: south-easterly flow (the TJ), and the larger south-westerly flow (East Africa Low Level Jet- EALLJ). This splitting is first seen in May, as evident in figure 1a and 1b (May panel in ERA5 and the

HadGEM-GC31-LL). The north-easterly stream forms the TJ with a clear axis from southeast to northwest first seen in April and October in both ERA5 and the HadGEM-GC31-LL model.

The mean wind speeds for 1981 to 2014 are shown for a point at mid Turkana channel (Figure 1d). In ERA5, they remain relatively high throughout the year with mean values ranging between 10 and about 13 m/s. While the CMIP6 ensemble mean similarly has a 2 m/s range between maximum to minimum mean values, the magnitude of the model values is lower throughout the year. The difference is largest from May to October, when the EALLJ is also evident in both the ERA5 and the HadGEM-GC31-LL model. During the May to October period, the spread of individual model values about the ensemble (standard deviation) is minimal, indicating that the majority of the models show stronger departure in values from ERA5. During the same climatological period, the BCC-ESM1 model exhibited climatological mean wind speeds ranging between 5 and 9 m/s with particularly low values in presence of the EALLJ, from April to September. In the BCC-ESM1 model, the EALLJ is merged with the TJ, hence the TJ appears to terminate within this Turkana region in this BCC-ESM1 model. This shortfall appears to be characteristic of most of the models that contribute to the ensemble. Further analysis in subsequent sections will set up thresholds that will isolate the models that exhibit the shortfall.

The southerly winds carry moisture into the region during northern summer time compared to other months of the year (illustrated by red shading in figures 1a to 1c) and coincides with a period in which the regions bordering the northwest of Kenya receives extended rainfall (Chamberlin, 2018). Considering the TJ is a major transporting agent for moisture into northwest of East Africa (Vizy and Cook 2019; Munday et al., 2020), simulated impacts of the TJ to rainfall are likely to be different in the reanalysis and in the CMIP6 models that show a weaker TJ during the season.

3.2 Spatial Structure in climatology of the TJ in CMIP6

The mean vertical structure of the lower atmosphere (surface to 500 mb pressure level) winds is analyzed along the Turkana channel in CMIP6 models (figure 2). In ERA5 as well as in the models, the relatively high-speed winds are located above the surface; wind speeds increase between the surface and 850 mb and then decrease with altitude. The center of intensity appears between 925 mb and 850 mb pressure levels near the middle of the Turkana channel following acceleration at this point (Patwardhan and Asnani, 1999; Indeje et al., 2001).

In JJAS, at the mid-Turkana area, ERA5 and both versions of the CNRM model exhibit the highest change in wind speeds from maximum (approximately 12 m/s) at 850mb to minimum (approximately 7 m/s) before 500 mb level is reached (figure 2a). Other models with relatively large changes with height, of more than 5 m/s, include HadGEM3-GC31-MM, MRI-ESM2-0, CESM2, FGOALS-f3-L, SAM0-UNICON, ACCESS-CM2, HadGEM3-GC31-LL, IPSL-CM6A-LR and CanESM5. The rest of the models show lower wind shears as mean winds are slower at the mid-Turkana channel. They show the center of intensity further away from the middle area of the Turkana channel. The models are namely BCC-ESM1, CAMS-CSM1-0, SAM0-UNICON, TaiESM1, MIROC6, NESM3, INM-CM4-8, and INM-CM5-0. In these models, high wind speeds fail

to extend up to mid-Turkana Channel, an apparent consequence of the TJ merging with the EALLJ during the JJAS season.

During the October to May months, the EALLJ is absent, the center of intensity in the wind speeds shifts northwards to mid-channel area, it is elevated, and has a vertical elongation up to about 825 mb (figure 2b). As the winds flow through the channel in absence of the EALLJ, they are displaced upwards by the gently rising slope indicated in shown topography below each panel. The vertical extension of the TJ core is accompanied by weaker vertical wind shear. The weakening shear with height appears pronounced in a set of models which exhibited the center of intensity further away from the middle area of the Turkana channel during JJAS season (BCC-ESM1, CAMS-CSM1-0, SAM0-UNICON, TaiESM1, MIROC6, NESM3, INM-CM4-8, and INM-CM5-0). This phenomenon indicates that while the winds begin to accelerate at mid-Turkana channel, the gain in wind speed is lesser in these models compared to ERA5.

Those CMIP6 models which have lower wind speeds in the lower-atmosphere are of lower resolution. Considering that a TJ characterized by high wind speeds that decrease aloft result from acceleration within the Turkana channel, the disparities between the ERA5 and some of the CMIP6 models are likely to result from TJ interaction with topography within the channel.

3.3 Mean vertical flow in the Turkana channel

Figure 3 shows the mean omega through the study period, plotted for the northwest to southeast axis parallel to the Turkana channel (for models with the omega data available and the same transect is used as in Figure 2). Other than in the HadGEM-GC31-LL and the two versions of the CNRM model, descending motions dominate the entrance of the Turkana channel during the JJAS season and the mid-channel area during the months of October to May in CMIP6 models. Relating these results with those in Figure 2 shows that descending motions dominate lower atmospheric levels where the intensity of the TJ is strong. The ERA5, HadGEM-GC31-LL and the two versions of CNRM model have relatively faster winds at mid-Turkana area during JJAS season following intense TJ core in the season.

Additionally, the influence of the elevated terrain is noticeable. In both the JJAS and October to May seasons, ascending motion emanates between the entrance and the mid-channel area where the floor of Turkana channel begins depicting an elevation, due to frictional interaction of the wind with the sloping floor of the Turkana channel. During JJAS season the TJ core accompanied by subsidence aloft is further to the southeast of the mid-Turkana channel. This allows low-level ascents manifesting at the TJ entrance to incline towards the middle and exit area of the channel with height as generation of the ascents diminish as surface elevation slopes downwards at Turkana channel exit. This further strengthens uplifts at the exit area in the deep troposphere. During October to May months, the TJ core accompanied by subsidence aloft is at the mid-Turkana channel area. Thus, ascents from the TJ entrance area are inhibited from lateral movement towards the mid-Turkana area. At TJ exit, vertical motions are generated by deceleration of winds that leads to build up of pressure at lower atmosphere.

Other than the ERA5 and the two CNRM models, other CMIP6 models show stronger ascending motion, potentially from enhanced blocked lower atmospheric flow at the mid-Turkana channel. The ERA5, HadGEM-GC31 and CNRM models appear to depict unblocked flow through the channel with pockets of near surface descending motion associated with faster wind speeds at the mid-Turkana channel area. During the months of October to May, the mid-channel descents are stronger. This suggests that although strong TJ intensity induces the subsidence in the Turkana channel, the interaction between the TJ and the Turkana channel influences the intensity of the TJ core.

3.4 Topography in CMIP6

Figure 4a shows that the Turkana channel is the largest topographic feature below the 850 mb level within the study area bounded by longitudes 33°E and 41°E and latitudes 2°S and 9°N. The floor of the channel at the entrance is roughly 980 mb in ERA5 and the CMIP6 models. The channel floor gently rises to between 945 and 960 mb at mid-channel area with walls of the channel rising to about 915 mb in ERA5 and the models with less than 1° longitudinal grid step size. In coarser resolution models, the floor of the channel rises to the level that matches or approximates that of the wall and therefore, the channel appears flattened. This phenomenon is more apparent in the CanESM5 and the BCC-ESM1 models.

Figure 4b shows the cross-section of the Turkana channel at each longitude. The channel narrows from about 500 to 100 square kilometers in both the ERA5 and the CMIP6 model datasets as one approaches the longitude 37°E from the channel entrance situated at around 41°E, within latitudes 2°S and 9°N. The INM, NorCPM1 and NorESM2-LM models attain this constriction at 38°E. Exiting at the 37°E longitude; the channel widens to about 200 square kilometers further to the west of this longitude according to the ERA5.

While the narrowing results in the formation of a constriction at the 37°E longitude, the changes between adjacent cross sections are varied in CMIP6 models compared to ERA5, consistent with results in Vizy and Cook (2019). Other than the HadGEM3-GC31-MM and MPI-ESM1-HR models, cross-sectional areas at some adjacent longitudes are maintained or least changed compared to the ERA5. Strikingly, CanESM5 exhibits higher cross-sectional area changes whenever a difference is observed at its relatively coarse spatial grid resolution. The results from ERA5 and the HadGEM3-GC31-MM and MPI-ESM1-HR which are two high-resolution CMIP6 models show that reducing the grid-step size increases topographic details being resolved and forms a narrowing Turkana channel.

The difference between the cross-sectional area of the channel at the entrance and exit of the jet is computed. Figure 5 shows the narrowing index for CMIP6 models as well as the horizontal resolution (longitudinal grid step size) of the model. Since the cross-sectional area entrance of the channel (42°E) in the ERA5 and all the CMIP6 models is about 800 square kilometers and reduces to about an eighth of this at the mid-channel, models with zero changes between adjacent longitudes have higher gradient whenever shape changes. Thus, a low index (Figure 5, y-axis), which is characteristic of low-resolution models with higher grid step sizes, characterizes steep change in terrain followed by blocks of wall between the adjacent longitudes with constant cross-section area between them.

The ERA5 has the highest narrowing index for the Turkana channel. It is followed by CMIP6 models of less than 1.5° resolution in which the index is either maintained or weakens in models with higher grid-step sizes. At greater than 1.5° resolution, the CMIP6 models scattered values for the index and show inconsistency in how the narrowing of the channel is lost with increasing coarseness in the topography. The CanESM5 model is an outlier, returning a high value of the quantity due to high rates of change associated with very large grid-step sizes and a smaller number of points in the channel (Figure 4b). Therefore, linking this result with those from Figure 3 indicates that CMIP6 models with resolution greater than 1.5° have steep walls along the floor and height of the channel. This is a likely source of the impediment on the smooth flow near the surface along the Turkana channel.

3.5 Topographic influence on the TJ in CMIP6

The association between the strength of the TJ and the shape of the Turkana channel represented by the narrowing index, is explored in this section by adjusting the thresholds for JJAS season maximum wind speed and vertical shear (between the point of maximum and minimum wind speed before reaching 500 mb). Figure 6 shows TJ counts for wind speeds at 850 mb in range 6 to 10 m/s and wind shear above the TJ core in range 2 to 6 m/s, for each model and its narrowing index.

Most models return a TJ with maximum wind speeds exceeding 6 m/s and vertical wind shear above the TJ core exceeding 2 m/s. Only the CMIP6 models INM and ACCESS-ESM have the TJ structure weaker than this category within the 35-year study period. Higher thresholds of 9 m/s at 850 mb and vertical wind shear of 5 m/s TJs are still common in the majority (17) of the 26 CMIP6 models. Nearly half of the CMIP6 models return zero TJ counts at stricter criteria of higher than 9 m/s maximum wind speeds and greater than 5 m/s vertical shears above the TJ core. Therefore, we consider those thresholds as optimal.

The optimum thresholds are surpassed in CMIP6 models having a high index for the shape of the Turkana channel such as HadGEM3-GC31-MM, CNRM and MRI. This is similar to the ERA5 which has the highest index (Figure 5) considering TJs whose core is characterized by at least 9 m/s maximum wind speeds which decrease by at least 5 m/s above. Referring to Figure 2, the mean TJ in ERA5 reaches higher values for maximum wind speeds at 12 m/s, decreasing by 7 m/s above the core. But CMIP6 models with low index for shape of the Turkana channel exhibit mixed TJ characteristics. For instance, the CNRM and FGOALS-f3-L models exhibit TJs when NorESM2-LM and INM models of comparable index for the Turkana channel, return zero TJ count considering the optimum thresholds for the TJ in CMIP6 models. There were 9 CMIP6 models with zero TJs and 4 models with thirty-five TJs reaching the optimum threshold in 35 JJAS seasons. The remaining 13 CMIP6 models occasionally exhibited TJs reaching the optimum threshold for a strong jet (maximum wind speeds of 9 m/s and decreasing aloft the core by at least 5 m/s).

The different CMIP6 models (coarser than 1.5° longitudinal resolution) with low narrowing index show a lower consistency in narrowing cross sectional area. Considering that the narrowing supports channeling of the winds and acceleration of the winds (Indeje et al., 2001), models with coarser than 1.5° longitudinal grid step size which occasionally exhibit weak TJ structure, are here found to be related to poor resolution

of the Turkana channel. These irregularities in the TJ strength could also influence rainfall at TJ exit, as the TJ is considered a moisture transport mechanism (Munday et al., 2020).

3.6 Relationship between TJ and East African Precipitation in CMIP6

The influence of the TJ on the climate of East Africa is shown using the composite anomalies of precipitation for the JJAS season (Figure 7). Mean precipitation anomalies are shown for strong TJs in the CMIP6 models as they best match TJ strength in the ERA5 (at least 9 m/s at the 850 mb and vertical wind shear of at least 5 m/s above TJ core) in the “jet” panel and also when the strength was weaker “no jet cases” panel.

JJAS is a major season with rainfall accumulation of up to 1,500 mm over the northwest regions of East Africa while other parts of the region remain generally dry (Camberlin 2018). This is the average condition, exhibited when the TJ strength remains regular. Fluctuations in the TJ strength which is common in nearly half of the CMIP6 models used, induce spatial distribution of dry and wet anomalies.

In Figure 7 (left panel), when a perennially weak TJ strengthens in model climatology, dry anomalies at the border region of the exit the Turkana channel are exhibited. Specifically, in the whole JJAS season (122 days), rainfall is suppressed by up to 122 mm below the climatological mean (~ 8% of the 1,500 mm), observed in CAMS-CSM1-0, BCC-CSM2-MR GFDL-CM4 and FGOALS-g3. The dryness extends up to the west of South Sudan, east of Central African Republic, northern Congo and to the west of Ethiopian Highlands. The increasing dry anomalies at the TJ exit area is associated with stronger inflow of air with low moisture content during this season through lower atmosphere. Furthermore, during a strong TJ, easterly flow is so strong that it inhibits southwesterly advection of moist air from equatorial Congo.

Conversely, wet anomalies characterize the immediate exit of Turkana channel and Ethiopian highlands in the CMIP6 models when perennially strong TJ weakens below the thresholds (Figure 6; right panel). Precipitation is enhanced by up to 1 mm more than the climatological mean in the models. Further to the west of South Sudan, in the Central African Republic and northern Congo, dry anomalies below the climatological mean are exhibited. This is likely associated with enhanced uplift of moist air that is transported from the Indian Ocean through the Turkana channel at TJ exit. In this case, pressure piles up at the immediate exit due to deceleration of winds and promotes zonal advection of moisture-laden air to the western regions of South Sudan (Vizy and Cook 2019). Furthermore, during a weak TJ, southwesterly advection of moist air from equatorial Congo is likely being promoted.

4 Summary And Conclusions

The TJ is a persistent jet stream that is observed throughout the year in the ERA5 data with seasonal mean wind speeds ranging between 11 m/s and 13 m/s at approximately 850 mb level. However, it varies appreciably in CMIP6 models with typical core speeds ranging between 5 and 9 m/s. The maximum wind speed at the core of the TJ in the ERA5 is highest during May to October months when the background

flow is southeasterly, while the majority of the CMIP6 models with coarse resolution show their minimum wind speeds during this period.

The period from June to September is characterized by strong vertical shear above the TJ core at the mid-Turkana channel and the presence of the EALLJ in both the ERA5 and CMIP6 models. In some models the EALLJ dominates, and there are high wind speeds (up to 9 m/s) closer to the entrance of the Turkana channel while the winds at the mid-channel area are too weak by up to 5 m/s. This is an indication that the TJ is merged with the EALLJ, which inhibits the strong winds from reaching mid-Turkana channel. In other months of the year, the EALLJ is inactive and the high wind speeds (up to 9 m/s) are located at mid-Turkana channel signifying the TJ core in CMIP6 models as is in ERA5. Furthermore, the core of the TJ appears vertically extended up to 700 mb in the models and reduces the magnitude of change between maximum wind speed at TJ core and minimum wind speeds found aloft at the mid-channel. The vertical wind profiles are therefore mixed in most CMIP6 models.

Analysis of vertical winds indicate that the mixed profiles of wind speed in the CMIP6 models is potentially related to ascending motion from the mid-Turkana channel that leads to the upward spread of relatively high wind speeds. The upward flow from the mid-channel could be enhanced by frictional interaction with the floor and wall of the Turkana channel and is pronounced in CMIP6 models with horizontal resolution of coarser than 1.5°. The frictional encounter of the wind flow with the floor of the Turkana channel appears as enhanced ascending motion from blocked flow at mid-Turkana channel. The enhanced ascend due to blocked motion is likely to result in heightening of precipitation. From this analysis, precipitation is enhanced up to 1 mm per day at exit of the TJ by the ascents in CMIP6 models with longitudinal grid step size higher than 1.5°.

This study provides insights on the representation of features of the TJ in the available CMIP6 models and ERA5 dataset. The results also reaffirm the importance of the TJ to the climate of East Africa by transporting moisture during the northern summer, an aspect also presented in other studies including Indeje et al. (2001), Nicholson (2016), Vizy and Cook (2019) and King et al. (2021). Additionally, we find that higher resolution CMIP6 models have a better Turkana channel characterized by consistent narrowing along the channel (through the narrowing index) which allows for smooth flow and acceleration of winds at mid-Turkana channel area. The study has demonstrated that for coarse model resolution with a low of at least 1.5°, the narrowing index is low and produces a TJ with high variability in its strength, location of core and vertical structure. The variation in strength, location and structure of the TJ translates to biases in the CMIP6 model rainfall climatology over Eastern Africa, leading to emergence of dry (wet) anomalies over the northwestern region of East Africa when the TJ is strong (weak). The enhancement of wet anomalies is up to 8% above the observed climatology at the immediate exit of the TJ when the jet stream is weaker.

These findings demonstrate the importance of realistically representing the topography details over the Turkana channel. This highlights the need for field studies to determine a realistic baseline for comparison of the observed climatology of the TJ and the relationship between the TJ and rainfall.

Furthermore, while an understanding of the TJ features can be drawn from some low-resolution reanalysis and models (e.g., Nicholson 2016, King et al., 2021), there is the need for increased resolution to realistically represent the TJ. The narrowing index provides a quantitative way to track improvement of high-resolution modeling to the narrowing shape of the Turkana channel, much needed to realistically represent the structure, position, strength of TJ and influence on rainfall in atmospheric models. The next steps for this work are to apply our findings to models with resolution hierarchy in controlled experiments and further explore the factors responsible for the inter-annual variability of the perennially weak TJ in the CMIP6 models.

Declarations

Acknowledgements

This work is part of outputs from the LaunchPAD (Priority on African Diagnostics) project, funded by the Foreign, Commonwealth and Development Office (FCDO) to create a Climate Model Evaluation Hub for Africa. The analysis in this work was done via JASMIN data cluster with datasets. We acknowledge the ECMWF for providing the ERA5 datasets, and the World Climate Research Programme Working Group on Coupled Modeling, for providing CMIP6 datasets to support this research.

Data Availability Statement

The ERA5 dataset analyzed in this work are available through,
https://cds.climate.copernicus.eu/cdsapp#!/home and CMIP6 data through the Centre for Environmental Data Analysis (CEDA), available here
https://catalogue.ceda.ac.uk/uuid/b96ce180077f4810abc4eef0e48901d9.

References

1. Acosta, R. P., and Huber, M. (2017). The neglected Indo-Gangetic Plains low-level jet and its importance for moisture transport and precipitation during the peak summer monsoon. Geophysical Research Letters, 44(16), 8601–8610. doi:10.1002/2017gl074440
2. Ba M.B, Nicholson S.E (1998). Analysis of convective activity and its relationship to the rainfall over the Rift Valley lakes of East Africa during 1983-1990 using the METEOSAT infrared channel. J. Clim. Appl. Meteorol. 10: 1250–1264.
3. Eyring, V., Bony, S., Meehl, G. A., Senior, C. A., Stevens, B., Stouffer, R. J., and Taylor, K. E. (2016). Overview of the Coupled Model Intercomparison Project Phase 6 (CMIP6) experimental design and organization, *Geosci. Model Dev.,* 9, 1937–1958, https://doi.org/10.5194/gmd-9-1937-2016.
4. Flohn H. (1964). On the causes of aridity of northeastern Africa. Würzburger Geograph. Arb. 12: 1–17.

5. Griffiths J. F. (1972). Climates of Africa. World Survey of Climatology, Vol. 10. Elsevier: New York, NY, 620 pp
6. Hart J. E, Rao G.V, Van De Boogaard H, Young J.A, Findlater J. (1978). Aerial observations of the East African low-level jet stream. *Mon Weather Rev* 106(12):1714–1724
7. Hartman A. T (2018) An analysis of the effects of temperatures and circulations on the strength of the low-level jet in the Turkana Channel in East Africa. Theor Appl Climatol 132:1003–1017. https://doi.org/10.1007/s00704-017-2121-x
8. Hersbach, H., Bell, B., Berrisford, P., Hirahara, S., Horányi, A., Muñoz-Sabater, J., Nicolas, J., Peubey, C., Radu, R., Schepers, D., Simmons, A., Soci, C., Abdalla, S., Abellan, X., Balsamo, G., Bechtold, P., Biavati, G., Bidlot, J., Bonavita, M., De Chiara, G., Dahlgren, P., Dee, D., Diamantakis, M., Dragani, R., Flemming, J., Forbes, R., Fuentes, M., Geer, A., Haimberger, L., Healy, S., Hogan, R.J., Hólm, E., Janisková, M., Keeley, S., Laloyaux, P., Lopez, P., Lupu, C., Radnoti, G., de Rosnay, P., Rozum, I., Vamborg, F., Villaume, S., Thépaut, J.N., (2020). The ERA5 global reanalysis. Q. J. R. Meteorol. Soc. 146 (730). https://doi.org/10.1002/qj.3803.
9. Hufman G.J, Adler R.F, Bolvin D.T, Gu G, Nelkin EJ, Bowman KP, Hong Y, Stocker EF, Wolf D.B (2007). The TRMM multisatellite precipitation analysis (TMPA): quasi-global, multiyear, combined-sensor precipitation estimates at fine scales. *J Hydrometeorol* 8:38–55. https://doi.org/10.1175/JHM560.1
10. Indeje M, Semazzi F.H.M, Xie L, Ogallo L.J, (2001). Mechanistic model simulations of the East African climate using NCAR regional climate model: influence of large-scale orography on the Turkana low-level jet. *J. Clim.* 14: 2710–2724
11. James, R., R. Washington, B. Abiodun, G. Kay, J. Mutemi, W. Pokam, N. Hart, G. Artan, and C. Senior, (2017). Evaluating climate models with an African lens. *Bull. Amer. Meteor. Soc.* doi:10.1175/BAMS-D-16-0090.1, in press.
12. Kilavi, M., MacLeod, D., Ambani, M., Robbins, J., Dankers, R., Graham, R., Todd, M. (2018). Extreme Rainfall and Flooding over Central Kenya Including Nairobi City during the Long-Rains Season 2018: Causes, Predictability, and Potential for Early Warning and Actions. Atmosphere, 9(12), 472. doi:10.3390/atmos9120472
13. King, J. A., Engelstaedter, S., Washington, R., Munday, C. (2021). Variability of the Turkana low-level jet in reanalysis and models: Implications for rainfall. Journal of Geophysical Research: Atmospheres, 126, e2020JD034154. https://doi.org/10.1029/2020JD034154
14. Kinuthia J.H (1992). Horizontal and vertical structure of the Lake Turkana Jet*. J. Appl. Meteorol*. 31: 1248–1274.
15. Kinuthia J. H, Asnani G.C. (1982). A newly found jet in North Kenya (Turkana Channel)*. Mon. Weather Rev.* 10: 1722–1728.
16. Krishnamurti, T. N., J. Molinari, and H. L. Pan (1976). Numerical simulation of the Somali jet. *J. Atmos. Sci*., 33, 2350–2362.
17. Levin N.E, Zipser E.J, Cerling T.E (2009). Isotopic composition of waters from Ethiopia and Kenya: insights into moisture sources for eastern Africa. *J Geophys Res* 114: D23306.

https://doi.org/10.1029/2009JD012166

18. Liu M, Westphal D.L, Holt TR, Xu Q, (2000). Numerical simulation of a low-level jet over complex terrain in southern Iran. Mon. Weather Rev. 128: 1309–1327.
19. McCann, J. C, (1995). People of the plow: An agricultural history of Ethiopia, 1800–1990. Milwaukee, WI: University of Wisconsin Press.
20. Mekonnen A, Thorncroft C.D, (2016). On mechanisms that determine synoptic time scale convection over East Africa. Int J Climatol 36:4045–4057. https://doi.org/10.1002/joc.4614
21. Mukabana J. R and Pielke R. A (1996) Investigating the influence of synoptic-scale monsoonal winds and mesoscale circulations on diurnal weather patterns over Kenya using a mesoscale numerical model. Mon Weather Rev 124:224–242. https://doi.org/10.1175/15200493(1996)124%3c0224:ITIOSS%3e2.0.CO;2
22. Nicholson S. E. (1996) A review of climate dynamics and climate variability in eastern Africa. In *The Limnology, Climatology and Paleoclimatology of the East African Lakes*, Johnson TC, Odada E.O (eds). Gordon and Breach: Toronto, Canada, 25–56
23. Nicholson, S. E., (2014). The predictability of rainfall over the Greater Horn of Africa. Part I. Prediction of seasonal rainfall. *J. Hydrometeorol.*, 33, 1011-1027, doi: 10.1175/JHM-D1129 13-062.1.
24. Nicholson S. E., (2016) The Turkana low-level jet: mean climatology and association with regional aridity. Int J Climatol 36:2598–2614. https://doi.org/10.1002/joc.4515
25. Njenga M., Leeuw J., O'Neill M., Ebanyat P., Kinyanjui M., Kimeu P., Adirizak H., Sijmons K., Vrieling A., Malesu M., Oduor A., and Dobie P. (2014). The need for resilience in the drylands of Eastern Africa. In Leeuw J., Njenga M., Wagner B., and Iiyama M (Ed) *Treesilience: An Assessment of the Resilience Provided by Trees in the Drylands of Eastern Africa.* World Agroforestry Centre Nairobi. DOI:10.13140/2.1.4118.5927
26. Ongoma, V., Chen, H., and Gao, C. (2017). Projected changes in mean rainfall and temperature over East Africa based on CMIP5 models. *International Journal of Climatology*, 38(3), 1375–1392. doi:10.1002/joc.5252
27. Otieno, V. O. and R. O. Anyah (2013). CMIP5 simulated climate conditions of the Greater Horn of Africa (GHA). Part II: projected climate. Clim. Dyn., 41 (7-8), 2099–2113, doi: 405 10.1007/s00382-013-1694-z.
28. Parry, J.; Echeverria, D.; Dekens, J. (2012). Maitima, J. Climate Risks, Vulnerability and Governance in Kenya: A Review; UNDP: New York, NY, USA, 2012; 78p. Available online: https://www.iisd.org/system/files/publications/climate_risks_kenya.pdf?q=sites/default/files/publications/climate_risks_kenya.pdf (accessed on 3 August 2021).
29. Patwardhan, S., Kulkarni, A. and Sabade, S. (2016). Projected Changes in Semi-Permanent Systems of Indian Summer Monsoon in CORDEX-SA Framework. *American Journal of Climate Change*, 5, 133-146. http://dx.doi.org/10.4236/ajcc.2016.52013
30. Philip, S., S.F. Kew, G.J. van Oldenborgh, F. Otto, S. O'Keefe, K. Haustein, A. King, A. Zegeye, Z. Eshetu, K. Hailemariam, R. Singh, E. Jjemba, C. Funk, and H. Cullen. (2018). Attribution analysis of the

Ethiopian drought of 2015. Journal of Climate 31 (6): 2465–2486. https://doi.org/10.1175/JCLI-D-17-0274.1.

31. Sun L.Q, Semazzi F.H.M., Giorgi F., Ogallo L. (1999) Application of the NCAR regional climate model to eastern Africa – 1. Simulation of the short rains of 1988. *J. Geophys. Res. Atmos*. 104: 6529–6548.
32. Taylor, K. E., Stouffer, R. J., and Meehl, G. A. (2012) An overview of CMIP6 and the experimental design, *B. Am. Meteorol. Soc.,* **93**, 485–498, https://doi.org/10.1175/BAMS-D-11-00094.1
33. Trewartha GT. (1981) The Earth's Problem Climates. *University of Wisconsin Press*: Madison, WI, 340 pp.
34. Uhe, P., Philip, S., Kew, S., Shah, K., Kimutai, J., Mwangi, E., Jjemba, E., (2018). Attributing drivers of the 2016 Kenyan drought. *Int. J. Climatol.* 38, 554–568.
35. Vizy, E. K., Cook, K.H. (2019) Observed relationship between the Turkana low-level jet and boreal summer convection. *Clim Dyn* **53,** 4037–4058. https://doi.org/10.1007/s00382-019-04769-2
36. Williams A. P, Funk C, Michaelsen J, Rauscher S. A, Robertson I, Wils T. H. G, Koprowski M, Eshetu Z, Loader N. J (2012). Recent summer precipitation trends in the Greater Horn of Africa and the emerging role of Indian Ocean Sea surface temperature. *Clim Dyn* 39:2307–2328. https://doi.org/10.1007/s00382-011-1222-y
37. Yang, W., Seager, R., Cane, M. A., and Lyon, B. (2015). The Rainfall Annual Cycle Bias over East Africa in CMIP5 Coupled Climate Models. *Journal of Climate*, 28(24), 9789–9802. doi:10.1175/jcli-d-15-0323.1

Figures

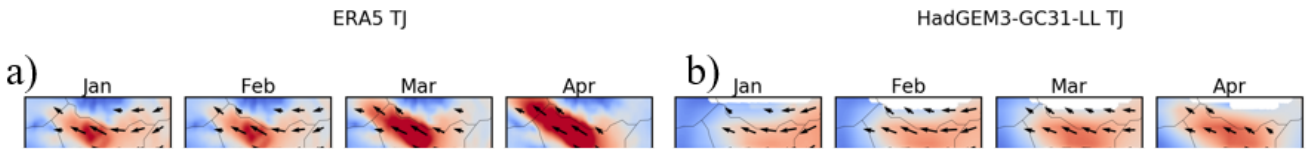

Figure 1

The 1980 to 2014 climatological moisture flux at 850 millibars (g/Kg/m/s), overlaid with mean wind vector at 850 millibars (m/s) for different datasets in plots a, b and c. Wind vectors indicate winds of at least 5 m/s. Green dot in the May subplot of each panel denotes a point 37°E, 3°N which is the model grid point closest to the Turkana area. In plot d, are ERA5, the 2 CMIP6 models and the CMIP6 ensemble mean

wind speed at the same level in each month of the year for the grid closest to 37°E, 3°N. Gray shaded region denotes +/- one standard deviation of the 26 models in each month around the ensemble.

Figure 2

The 1980 to 2014 climatological wind speeds from surface to 500 mb in m/s, along a transect parallel to the Turkana Channel in Northwest (31°E and 8°N) to Southeast (43°E and 2°S) direction through a point at center of the channel (37°E and 3°N), centered around June to September (plot a) and October to May season (plot b). Topography is illustrated in the bottom of each subplot in brown.

Figure 3

Climatology of vertical cross-section of the June to September (left plot) and October to May (right plot) omega (Pascals per second) for the years 1980 to 2014 along the Northwest (31°E and 8°N) to Southeast (43°E and 2°S) transect of the Turkana channel. Topography is illustrated in the bottom of each subplot in brown.

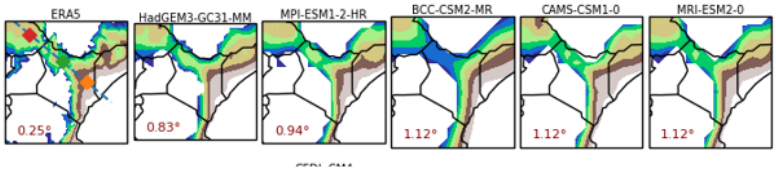

Figure 4

a. Surface elevation in ERA5 and the CMIP6 models over the Turkana channel area, with elevation above 850 mb level masked out. The in-plot texts indicate the model longitudinal grid step size. The blue dotted line in the ERA5 panel show a transect parallel to the Turkana Channel in Southeast (entrance; cyan) to Northwest (exit; red) direction through a point at center of the channel (green; 37°E and 3°N)

b. Estimated cross sectional area of Turkana Channel -TC (in square kilometers) at each longitude between latitudes 2° S to 9° N.

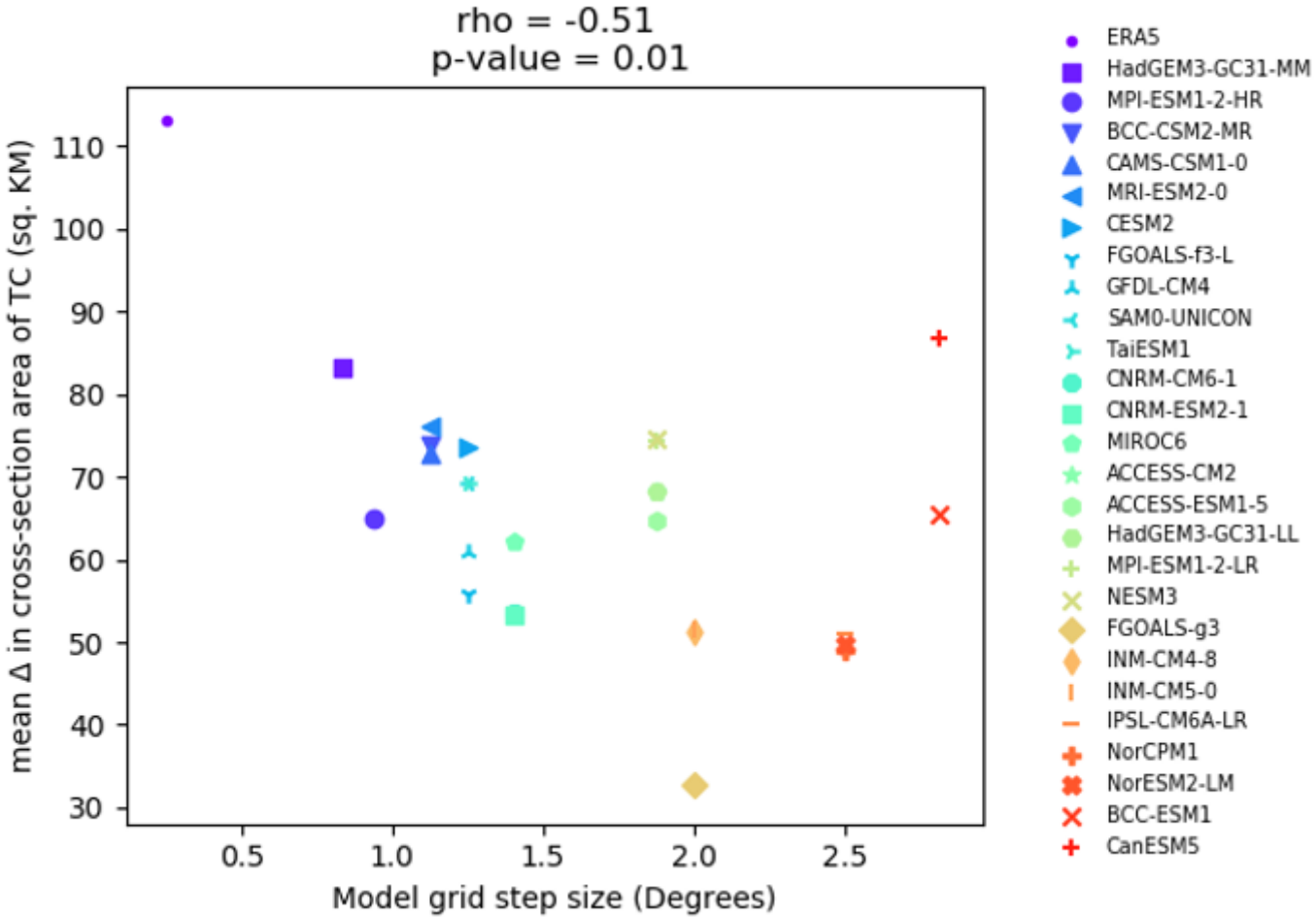

Figure 5

Mean zonal change in cross-sectional area of Turkana channel estimated between longitudes 33° E and 42° E, each longitude spanning between latitudes 2° S to 9° N; referred to as the narrowing index in this paper. The quantity is computed for different models on their native grid whose longitude grid spacing are shown in the x-axis. The Pearson product moment correlation coefficient (rho) between the narrowing index and the horizontal grid resolution shows significant correlation at the 95% confidence level (p-value < 0.5)

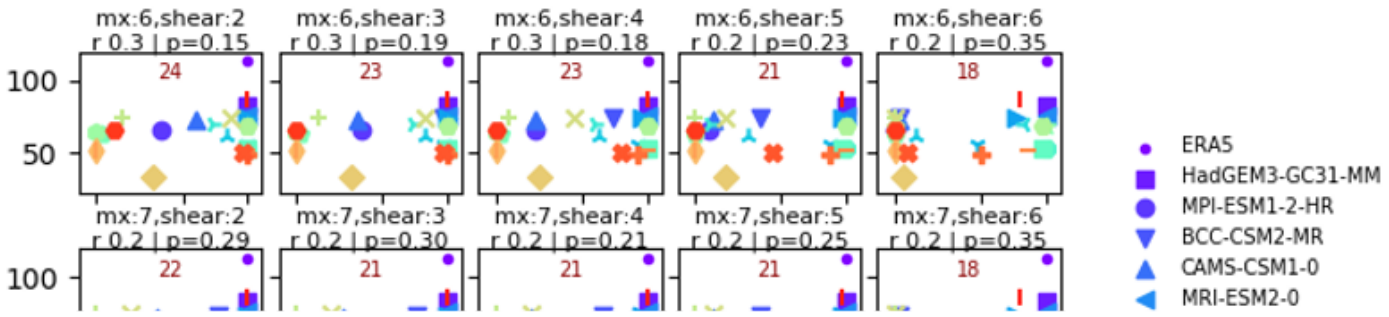

Figure 6

Dependence of the TJ occurrence on the narrowing index. Counts are made for the TJ of maximum wind speeds and highest decrease between 850mb and point of minimum below 500 mb, shown in the title of each subplot. Also shown in text are spearman's rank correlation and p-value between TJ counts and narrowing index. The number of models returning more than zero (0) TJ count is shown in inner text

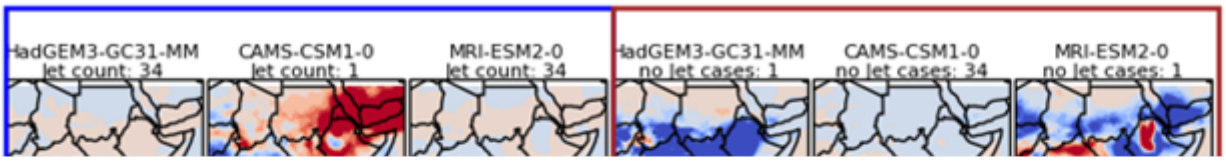

Figure 7

Composite anomalies for precipitation during the June to September season for the years 1980 to 2014. Left panel shows the anomaly when the climatological precipitation values are subtracted from mean precipitation during jet occurrence (TJ core speeds at least 9 m/s and decreases above the core by at least 5 m/s). Right panel shows the anomaly when the mean precipitation values are subtracted from mean precipitation for no jet occurrence.